Title

Seasonal variations in the Rayleigh-to-Love wave ratio in the secondary microseism from colocated ring laser and seismograph

Journal

Journal of Geophysical Research: Solid Earth, 121(4)

ISSN

2169-9313

Authors

Tanimoto, Toshiro
Hadziioannou, Céline
Igel, Heiner
et al.

Publication Date

2016-04-01

DOI

10.1002/2016jb012885

Peer reviewed

Seasonal variations in the Rayleigh-to-Love wave ratio in the secondary microseism from co-located ring laser and seismograph

Toshiro Tanimoto[1]*, Céline Hadziioannou[2], Heiner Igel[2], Joachim Wassermann[2], Ulrich Schreiber[3], André Gebauer[3], and Bryant Chow[2]

1. Department of Earth Science and Earth Research Institute, University of California, Santa Barbara, California 93106, USA.
2. Department of Earth and Environmental Sciences, Ludwig-Maximilians-University, Theresienstr. 41 80333 Munich, Germany
3. Forschungseinrichtung Satellitengeodaesie, Technische Universitaet Muenchen - Fundamentalstation Wettzell, Sackenrieder Str. 25, D-93444 Bad Koetzting, Germany

*Corresponding author: Email toshiro@geol.ucsb.edu

Abstract

Monthly variations in the ratio of Rayleigh-to-Love waves in the secondary microseism are obtained from a co-located ring laser and an STS-2 seismograph at Wettzell, Germany. Two main conclusions are derived for the Rayleigh-to-Love wave kinetic energy ratios in the secondary microseism; first, the energy ratio is in the range 0.8-0.9 (< 1.0) throughout a year except for June and July. It means that Love-wave energy is larger than Rayleigh-wave energy most of the year by about 10-20 percent. Second, this ratio suddenly increases to 1.0-1.2 in June and July, indicating a larger fraction of Rayleigh-wave energy. This change suggests that the locations and behaviors of excitation sources are different in these months.

1. Introduction

It has generally been assumed that there is more Rayleigh-wave energy than Love-wave energy in seismic noise within the microseismic frequency band (0.05-0.4 Hz). This is because the mechanism for exciting Rayleigh waves by ocean waves was established by Longuet-Higgins [1950] and it naturally explained an important feature of double-frequency bands in the microseisms, i.e. the primary and the secondary microseisms. On the other hand, the mechanism of exciting Love waves has never been clear. With the development of dense seismic arrays of broadband stations, however, it is becoming clear that there is surprisingly a large fraction of Love waves in the microseisms [e.g., Nishida et al., 2008]. This paper lends support to these results and points out a new feature in the seasonal variation that is contained in the energy ratio between Rayleigh waves and Love waves.

Our basic motivation for this study was that there are surprisingly few data that constrain the energy partition between Rayleigh waves and Love waves in the microseisms. This applies to both the primary microseism (about 0.05-0.07 Hz) and the secondary microseism (about 0.10-0.40 Hz). Answering this question has not been easy because source areas are not well localized [e.g., Chevrot et al., 2007] and seismic arrays that are needed to understand the sources have been scarce until recently [e.g., Friedrich et al., 1998].

In one of few contributions to this problem, Nishida et al. [2008] estimated the ratio of Love waves to Rayleigh waves using an array of tilt meters in Japan. Since phase velocities of Rayleigh and Love waves are different, separation of these two types of waves is possible by an array study. Their conclusion was that there was more Love-

wave energy than Rayleigh-wave energy below 0.1 Hz but it changed above 0.1 Hz and Love-wave energy became about 50 percent of Rayleigh-wave energy. Similar studies have been conducted in other regions recently that take advantage of a number of seismic arrays and we expect to see more results in this line of work in the near future [e.g., Riahi et al., 2013; Juretzek and Hadziioannou, 2015].

In this study, we take a different approach; we use a unique set of instruments at Wettzell (WET), Germany, where an STS-2 seismograph and a ring laser [Schreiber et al., 2009; Schreiber and Wells, 2013] are co-located. We estimate the amount of Rayleigh waves from the vertical component seismograph (STS-2) and the amount of Love waves from the ring laser. The ring laser records the rotation in the medium and the records are dominated by SH-type waves, thereby allowing us to measure the amount of Love waves.

We already reported our basic method and preliminary results [Tanimoto et al., 2015]. Since then we have extended our analysis to temporal changes in the Rayleigh-to-Love wave ratios for the secondary microseism. In this study, we also correct for the minimum resolution problem (section 3.2) that was not included in the previous study. Because of the lack of this correction, our previous work led to some overestimates for the amount of Love waves. After this baseline correction, we find that the ratio of Love-wave kinetic energy to Rayleigh-wave energy is about 0.8-0.9 (<1.0) except for June and July. In these two months, this ratio increases to about 1.0-1.2. These two points are the main conclusions of this study.

We present the general characteristics of data at WET in section 2, our approach in section 3, the main results in section 4, and some discussions in section 5.

2. Data at Wettzell

In this study, we use a three-component seismograph (STS-2) and a ring laser at WET. For details on ring laser instruments, we refer the reader to Schreiber and Wells [2013]. The ring laser at WET measures the vertical (z) component of rotation rate $\dot{\omega}_z = (1/2)(\nabla \times \mathbf{v})_z$ where the dot denotes time derivative and $\mathbf{v}$ denotes ground velocity. There is a small possibility that tilt can contaminate the data, thus signals related to P-SV type seismic waves (mostly Rayleigh waves) may get mixed in, but Pham et al. [2009] showed that the effects of tilt are negligible even for large earthquakes. We also examined this point in Tanimoto et al. [2015] and showed that the contribution from tilt is quite small (less than 0.1 percent) for seismic noise. Therefore, dynamically induced tilt, generated by seismic signals, does not seem to cause any serious contamination in the rotation measurement. There have been some reports of seasonally changing tilt due to thermoelastic effects [e.g., Prawirodirdjo et al., 2006; Ben-Zion and Allam, 2013] whose magnitudes are large (~ 0.1 micro-radians). But their main frequency bands (~ 1 day) are three-orders of magnitude lower than that of microseisms (0.05-0.40 Hz). Because of this difference in frequencies, these tilts are not relevant to seasonal variations in our results. In practice, the ring laser data in the frequency range of our analysis may be considered to be free from tilt contamination.

We rely on the vertical-component seismograph to estimate the amount of Rayleigh waves but we also examine two horizontal components. Since both Rayleigh waves and Love waves are present in horizontal-component seismograms, it is hard to obtain clean information for each type of wave separately. But the comparison between the ring laser data and the horizontal seismograms provides some constraints. For

example, our choice for the frequency range of this study was from 0.13 Hz to 0.30 Hz; this was influenced by comparison between ring-laser data and horizontal-component seismograms as ring-laser derived transverse accelerations (pure Love waves) and the horizontal-component accelerations (containing both Rayleigh and Love waves) cannot be different very much. We found large deviations for frequencies 0.10-0.12 Hz, for example, that were clearly anomalous. We thus chose the minimum frequency of our analysis at 0.13 Hz.

We analyzed the ring laser data at WET from 2009 to 2015. Fig. 1 shows the location of Wettzell, in the Bavarian forest close to the Germany-Czech border. The ring laser provides time series of rotation rate (unit radian/sec) and we used data that had 20 samples per second. Over this six-year span, we computed the power spectral density (PSD) for every 15 minutes (Fig. 2a). Each dot in Fig. 2a shows an averaged PSD value between 0.1 and 0.4 Hz. PSD was computed by $|F(\omega)|^2 /T$ where $F(\omega)$ is the Fourier spectra at an angular frequency ω and T is the length of time series (15 minutes). To be more precise, we applied the Hanning window to time domain signals, computed PSD using the above formula and multiplied the correction factor 8/3 which compensates the reduction of power caused by the Hanning window [e.g., Osaki, 1976].

These PSD data are folded onto one-year interval using the Julian days in Fig. 2a. There are points above the maximum value in this figure, most of which were caused by earthquakes. As our goal is to study seismic noise, this study will focus on this small-amplitude range in Fig. 2a. However, even in the data shown in Fig. 2a, there may be some effects from earthquakes that are buried in the scatter of points. We remove these effects by using two earthquake catalogues.

117 Seasonal variations are obvious in the raw PSD data (Fig. 2a). The monthly
118 averages and error bars (one standard deviation) are shown in Fig. 2b (left). The
119 amplitudes in winter are about 8-10 times larger than the amplitudes in summer. In the
120 right panel of Fig. 2b, we show the results of a similar analysis for the vertical-
121 component seismograms. Since the ring laser data (RLAS) mostly contain Love-wave
122 energy and the vertical seismograph data mostly contain Rayleigh-wave energy, we can
123 directly confirm similar seasonal variations in both types of waves.

124 **3. Approach**

125 **(3.1) Monthly averages**

126 We first create the monthly-averaged Fourier amplitude curves both for the
127 vertical component seismograms and for the ring laser data. As the goal of this study is to
128 estimate the amount of Love waves and Rayleigh waves in seismic noise, it is essential to
129 make these data free of earthquake effects as much as possible.

130 We used two earthquake catalogues to remove earthquake effects. One is the
131 Global Centroid Moment Tensor catalogue (GCMT, www.gcmt.org) which includes all
132 events larger than M=5.5 where M is the Moment magnitude. This catalogue also
133 contains some smaller events than M=5.5. In addition, we used a regional catalogue from
134 the European-Mediterranean Seismological Center (EMSC, www.emsc-csem.org) in
135 order to remove earthquake effects for events larger than M=4.5 within the distance of
136 1000 km from WET.

137 Technically we eliminate the portions in seismograms from our data set using the
138 origin time of earthquakes and time length that we assign based on the size of

earthquakes; specifically, for M=8 or larger events anywhere in the world, we removed a whole day (24 hours) after their origin time. For M=6-8, we removed 12 hours, and for events less than M=6 (M=4.5-6), we removed 6 hours from the origin time.

Fig. 3 shows the monthly averaged spectral amplitudes for vertical component data. We show the average of 15-minute long Fourier amplitudes, not the power spectral density plotted in Fig. 2a and Fig. 2b. A number by each line indicates a month. We use 1 for January, 2 for February, 3 for March and so forth. The winter months (1, 2, 12) are shown in blue and the summer months (6, 7, 8) are shown in red. The spring months (3, 4, 5) are in green and the fall months (9, 10, 11) are in yellow (with black circles). One can see that these amplitudes are relatively stable both in summer and in winter but vary quickly in spring and fall months. In this plot, we can also see the peaks for the primary microseism at about 0.05-0.07 Hz and the predominant peaks for the secondary microseism between 0.1 and 0.3 Hz. The fact that we observe smooth monthly transitions in spectral amplitude indicates that earthquake effects were removed to a large extent.

Fig. 4 shows the results of a similar analysis to the ring laser data. Use of the numbers for months and the color scheme for each month are the same with Fig. 3. The basic characteristics in monthly variations are the same with seismic data; the spectra in winter months (1, 2, 12) and those in summer months (6, 7, 8) are relatively stable. Amplitudes in spring months (3, 4, 5) and fall months (9, 10, 11) show quick transitions between the two end-member seasons, i.e., summer and winter.

(3.2) Baseline correction

We have noted that the ring laser data hit the minimum resolution limit in the analysis (Fig. 4). The dashed (horizontal) line in Fig. 4 indicates this limit that we refer to as the baseline (or a threshold) hereafter. Existence of this minimum resolution is the reason that we cannot observe the peaks for the primary microseism (about 0.05-0.07 Hz, Fig. 4). This lack of the peaks is in contrast with Fig. 3 (from STS-2 vertical data).

In order to take care of this problem, we reanalyzed data and determined this baseline value. Fig. 5 shows an example of such efforts where we focused on small-amplitude summer days in 2010 (Julian days from 214 to 226). For the time interval indicated by the red-dash box in the top panel (Fig. 5), we computed Fourier spectra for frequencies up to 0.5 Hz (bottom panel in Fig. 5). These Fourier amplitudes show a clear peak associated with the secondary microseism (its maximum is about 0.22-0.24 Hz because this is summer) but amplitudes are flat below about 0.15 Hz. This feature indicates that we have hit the minimum resolution for the ring laser. The mean and the standard deviation for amplitudes within a box (solid horizontal line in the bottom panel of Fig. 5) were computed using data below 0.1 Hz and led to an estimate of 0.753 ± 0.041 prad/s for the baseline value. The unit is pico-radian per second. Further analyses from other time intervals led to an estimate of the baseline to be about 0.75-0.80 prad/s. Hereafter, for most figures in this paper, we show the results with the baseline value of 0.80 prad/s. The only exception is that the final monthly variation results will show the effects from an alternative choice of this value.

We recalculated the Fourier amplitudes of the ring laser data using this baseline value (A_{BL}) by

$$U_{rot} = \sqrt{A_{RL}^2 - A_{BL}^2} \quad (1)$$

where U_{rot} is a corrected rotation-rate amplitude and A_{RL} is an uncorrected Fourier amplitude shown in Fig. 4. The underlying assumption is that seismic noise (our signal) is independent of the cause of this minimum resolution.

(3.3) Conversion to acceleration

Monthly spectral amplitudes from the seismometers (Fig. 3) and the ring laser (Fig. 4) are in different units and cannot be compared against each other directly. In order to compare using the same unit, we convert these data to acceleration. Since the vertical-component data from STS-2 are in ground velocity, a simple multiplication of angular frequency converts spectral amplitudes in Fig. 3 to vertical accelerations.

For the rotation spectra, we need a few more steps of processing. We use the relation that a multiplication of 2C to the rotation spectra, where C is the local Love-wave phase velocity, converts the rotation-rate data to surface transverse acceleration. This relationship was originally pointed out by Pancha et al. [2000] for two earthquakes and later used by Igel et al. [2005], Igel et al. [2007], Ferreira and Igel [2009], Kurrle et al. [2010] and Hadziioannou et al. [2012]. This processing assumes that Fourier amplitude spectra for the ring laser data consist of the fundamental-mode Love waves only. This assumption is only approximate as body waves and higher mode surface waves have been identified in seismic noise; however, since the excitation sources for seismic noise are quite shallow, seismograms are dominated by fundamental-mode surface waves and thus we believe this assumption is justified to a large extent.

In order to apply this relation to rotation data, we need to know the local Love-wave phase velocity at WET. In this study, we use an earth model reported by Fichtner et al. [2013], derived for the European continent; we used its structure at WET and computed theoretical Love-wave phase velocities for further analysis. Fig. 6 shows the P-wave and S-wave velocity models at WET. It is an anisotropic (transversely isotropic) model and Fig. 6 shows PV, PH, SV and SH velocities [e.g., Takeuchi and Saito, 1972]. The bottom panel of Fig. 6 shows Love-wave phase velocity for this model up to 0.45 Hz. Love-wave phase velocity is about 3.2-3.3 km/s but it has a uniformly decreasing trend with frequency in the frequency band of this study (0.1-0.4 Hz).

Fig. 7 shows comparisons between surface accelerations for the months of January, April, July and October. Each panel contains four curves. Red lines are surface transverse accelerations, obtained by multiplying 2C to the rotation spectra (after baseline correction of 0.8 prad/s). Blue lines are vertical accelerations obtained from vertical spectral amplitudes in Fig. 3. Green lines and black lines are surface accelerations derived from the NS component and the EW component of seismic data.

Comparison between Fig. 3 and Fig. 4 shows that the peak frequency in the rotation data (Fig. 4) appears to be shifted toward higher frequency with respect to the peak in the seismic data (Fig. 3). The peak locations match in Fig. 7, because the multiplication by 2C moves the rotation peak toward lower frequencies. This overall match in peak frequencies seems to support that the adopted seismic model for WET is quite reasonable.

We also note in Fig. 7 that amplitudes of transverse acceleration (red) are quite close to amplitudes of horizontal acceleration from the NS (green) and EW (black)

components. Since the NS and EW components in seismic data should contain both Rayleigh waves and Love waves, they may differ to some extent but should have similar amplitudes. The fact that they are all close in these linear plots suggests that our two assumptions on the earth model (Love-wave phase velocity) and on the predominance of fundamental-mode Love waves are reasonable assumptions.

However, we see some discrepancies in the low/high frequency ends in Fig. 7. In the low frequency end of Fig. 7, below about 0.12 Hz, we find large transverse acceleration (from rotational measurements) and much smaller horizontal accelerations (from the NS and EW seismographs). For example, transverse acceleration is 3-4 times larger than horizontal accelerations at 0.1 Hz at face value. This difference suggests inconsistency because transverse acceleration contains Love-wave energy while horizontal accelerations contain both Rayleigh-wave and Love-wave energy. Considering the fact that the same Love-wave energy is in both data, such a large transverse acceleration in comparison to horizontal accelerations seems problematic.

We believe this large deviation is most likely caused by the minimum resolution problem we discussed in section (3.2). For amplitudes near the baseline level (we used 0.8 prad/s), the correct signal level is hard to estimate from the use of equation (1) because there always exists some noise in addition to signals. When the signal level is much higher than the baseline value such as those in winter months, the correction by equation (1) works very well. In fact the corrected signals in winter are slightly smaller but are close to the original amplitudes (as in Fig. 4). Amplitude behaviors in Fig. 7 suggest that the transverse acceleration may contain some anomalous features below about 0.12 Hz and also above 0.30 Hz especially for summer months. Therefore, in the

250 following analysis, we choose to analyze data in the frequency range 0.13-0.30 Hz only,
251 where we do not see large deviations of transverse acceleration from two horizontal
252 accelerations.

253 **4. Rayleigh-to-Love wave ratio in the secondary microseism**

254 **(4.1) Ratio of surface acceleration**

255 We first measure the surface-amplitude ratios between vertical accelerations and
256 transverse accelerations. This is simply done by taking the ratio of the blue curves to the
257 red curves in Fig. 7. These ratios for each month are plotted in Fig. 8 (top) using the same
258 color scheme as in Fig. 3 and Fig. 4. The abscissa is frequency and varies from 0.13 Hz to
259 0.30 Hz. The ordinate is the Rayleigh-to-Love ratio whose range is from 0.6 to 1.6. Most
260 values exceed 1 in Fig. 8, especially near the spectral peak range within 0.15-0.25 Hz.
261 The values from summer (red) particularly stand out near their maximum frequency
262 range about 0.22-0.23 Hz. On the average, the ratios between Rayleigh waves (vertical)
263 to Love waves (transverse) are about 1.1-1.2. This ratio should be the same with ground
264 velocity and displacement.

265 **(4.2) Ratio of kinetic energy**

266 Next we convert these surface amplitudes to the kinetic energies of Rayleigh and
267 Love waves. Our procedure proceeds as follows; we compute the eigenfrequencies and
268 eigenfunctions of Rayleigh and Love waves for the seismic structure in Fig. 6. Examples
269 of eigenfunctions at 0.20 Hz are shown in Fig. 9; the red solid line is the eigenfunction
270 $W(z)$ of Love-wave fundamental mode. The blue and green solid lines are the vertical
271 $U(z)$ and horizontal eigenfunction $V(z)$ of Rayleigh-wave fundamental mode. The

depth coordinate z is from 0 (surface) to infinity and is positive downward. These eigenfunctions are defined for displacement. In our definition, a Love-wave eigenfunction $W(z)$ for an angular eigenfrequency ω and a wavenumber (k_x, k_y) is related to displacement as [e.g., Takeuchi and Saito, 1972]

$$u_x = -i\frac{k_y}{k}W(z)e^{i(\omega t - k_x x - k_y y)}$$

$$u_y = -i\frac{k_x}{k}W(z)e^{i(\omega t - k_x x - k_y y)}$$

$$u_z = 0$$

where the wavenumber vector defines the direction of propagation. A Rayleigh-wave eigenfunction $U(z)$ and $V(z)$ are related to displacement by

$$u_x = -i\frac{k_x}{k}V(z)e^{i(\omega t - k_x x - k_y y)}$$

$$u_y = -i\frac{k_y}{k}V(z)e^{i(\omega t - k_x x - k_y y)}$$

$$u_z = U(z)e^{i(\omega t - k_x x - k_y y)}$$

Dashed lines in Fig. 9 are the eigenfunctions of an isotropic medium when we averaged two P waves (PH and PV) and two S waves (SH and SV). Small differences between the anisotropic model and the isotropic model exist but our results are mostly insensitive to the anisotropy of the medium.

Using the surface acceleration ratios in Fig. 8 (top), we arrange the relative surface amplitudes of eigenfunctions between vertical and transverse components (U/W) and evaluate the kinetic energy integrals defined by

$$E_L = \omega^2 \int_0^\infty \rho W(z)^2 dz$$

$$E_R = \omega^2 \int_0^\infty \rho \{U(z)^2 + V(z)^2\} dz$$

for Love waves and Rayleigh waves. Ratios of these kinetic energy integrals (E_R / E_L) are plotted in Fig. 8 (bottom). These ratios become smaller than the surface acceleration ratios because Love waves energy penetrates slightly deeper than Rayleigh wave energy for the same frequency (Fig. 9). The average of the kinetic energy ratios becomes slightly smaller than 1.0 (Fig. 8, bottom).

The integrated kinetic energy ratios over two frequency bands are shown in Fig. 10. The abscissa is month denoted by numbers from January (1) to December (12). The ordinate is the kinetic energy ratio. The blue curve shows the ratio for the frequency band from 0.13 to 0.25 Hz where we find the amplitude peaks of the secondary microseism. The red line shows the case when we extend the highest frequency range from 0.25 Hz to 0.30 Hz. This case maintains the shape in monthly variations but the whole curve is shifted to lower values because the ratios are small between 0.25 Hz and 0.30 Hz.

A characteristic feature in Fig. 10 is the relatively constant ratio except for June and July. The blue curve (0.13-0.25 Hz) shows that the ratios are about 0.9 (0.8-1.0) most of the year except June and July. Therefore, except for these two months, there is approximately 10 percent more Love-wave energy than Rayleigh-wave energy. In the

frequency band 0.13-0.30 Hz (red curve), the ratio is about 0.8, meaning Love-wave energy is about 25 percent larger than Rayleigh-wave energy. Therefore, this energy ratio depends on the frequency range but Love-wave energy is always slightly larger than Rayleigh-wave energy.

The increase of ratios for June and July is about 20-30 percent in both frequency ranges. This feature seems to be relatively robust in our results.

(4.3) Effects of baseline values

As we discussed in section (3.2), the ring laser data have the minimum resolution limit and in our unit of Fourier amplitude, it is about 0.75-0.80 prad/s. Our results in Fig. 8 and Fig. 10 were derived for the baseline (threshold) value of 0.8. Fig. 11 compares the kinetic-energy ratios for the baseline values of 0.7 and 0.8. We also included standard deviations for the results with 0.8. Standard deviations for the baseline value of 0.7 (red) are about the same and are not plotted here to avoid clutter. Both curves are for the frequency range 0.13-0.25 Hz and the blue curve is the same as the one in Fig. 10.

Fig. 11 shows that if we choose the baseline value of 0.7, the jump in the Rayleigh-to-Love wave ratio almost disappears. However, our best estimate of the baseline value is 0.75-0.80 (prad/s) and the baseline value is unlikely to be close to 0.70. For the baseline value of 0.75, the jump will be smaller than that for 0.80 but it is still about 20 percent. Thus we believe that there is a jump in the kinetic energy ratio in June and July, which reaches about 20-30 percent.

There is a hint of small Rayleigh-to-Love wave ratio in May (5) and August (8) in Figs 10 and 11. This could be true but the size of uncertainties weakens the significance

of these features. We do not think that the lower ratios in May and August are robust features in our results.

5. Discussion and Conclusion

We have demonstrated that a co-located ring laser and a three-component seismometer (STS-2) at WET allowed us to separate Rayleigh waves and Love waves in the secondary microseism (0.13-0.30 Hz) and enabled us to estimate their kinetic energy ratios. We found that the Rayleigh-to-Love wave energy ratio is smaller than 1 most of the year. However, this ratio depends on a chosen frequency band; in the high-amplitude range of secondary microseism (0.13-0.25 Hz), this ratio was about 0.9. This ratio means that there is approximately 10 percent more Love-wave energy than Rayleigh-wave energy. In a slightly wider frequency band, 0.13-0.30 Hz, this ratio became about 0.8, indicating that there was about 25 percent more Love-wave energy. While our estimates contain some uncertainties, Love-wave kinetic energy seems to be consistently larger than Rayleigh-wave energy for the secondary microseism. These are relatively robust results but they were derived based on some assumptions and limitations in data. We will discuss three points below: (5.1) implications of large Love-wave energy, (5.2) limitations from the minimum resolution, and (5.3) a need for a local seismic structure.

(5.1) Implications of Large Love-wave energy

A large partition of Love-wave energy with respect to Rayleigh-wave energy poses a challenge to our understanding of the excitation and propagation of seismic energy in the secondary microseism. The Longuet-Higgins mechanism, the wave-wave interactions of ocean waves [Longuet-Higgins, 1950], is generally accepted to be the main mechanism of excitation but because it is equivalent to a vertical force, it only

354 excites Rayleigh waves for a layered medium. Even in the real three-dimensional Earth, it
355 cannot be an efficient excitation source for Love waves. One of the main arguments to
356 explain a large amount of Love-wave energy has been to invoke Rayleigh-to-Love wave
357 conversion at the ocean-continent boundary. This structural effect should be important as
358 the structural contrast at ocean-continent boundaries is generally sharp; on this point there
359 have been some careful studies by using numerical simulations (e.g., Gualtieri et al.,
360 2015) and undoubtedly there will be more such studies to come.

361 The question raised by our results is whether such conversion processes alone can
362 explain a larger fraction of Love waves than Rayleigh waves in the secondary
363 microseism. The wavelengths of these seismic waves are typically 10-30 km (period 5-10
364 seconds) and thus are not necessarily short in comparison to typical size of crustal
365 heterogeneity. Scattering effects cannot be ignored but their severity may not be as strong
366 as it would lead to an equi-partition of energy between Rayleigh and Love waves.
367 Therefore, a large fraction of Love-wave energy in our results seems to suggest that there
368 must be processes of Love-wave generation through the interactions of ocean waves with
369 the solid earth; such interactions can be quite large close to the coast as propagating
370 ocean waves in shallow depths can exert horizontal forces on the solid earth [e.g., Saito,
371 2010].

372 Ardhuin et al. [2015] presented an attractive hypothesis of explaining the hum
373 [e.g., Suda et al., 1998; Kobayashi and Nishida, 1998; Tanimoto et al., 1998] and the
374 microseisms by a unified mechanism, but their arguments mostly applied to Rayleigh
375 waves only. Our results indicate that the situations may be not so simple, as there is a
376 large fraction of Love waves in the microseism. A similar conundrum exists for the

377 toroidal hum whose source has not been understood very well [e.g., Kurrle and Widmer-
378 Schnidrig, 2008].

379 **(5.2) Limitations from the minimum resolution limit**

380 Monthly variations in the Rayleigh-to-Love wave energy ratio showed an increase
381 in June and July by about 20-30 percent, regardless of the chosen frequency band.
382 However, the size of this energy increase was dependent on the choice of the baseline
383 value. Among the preferred range of this value, 0.75-0.80 prad/s, this jump varied
384 between about 20 and 30 percent. This estimate cannot be improved unless the baseline
385 value (minimum resolution value for rotation) will be reduced further.

386 The minimum resolution limit (baseline) was also the reason that we could not
387 conduct similar analyses to the primary microseism (0.05-0.07 Hz). Monthly amplitudes
388 in Fig. 4 suggest that if this limit can be lowered by a factor of five through instrumental
389 improvement, we can observe the primary microseism and conduct similar analyses on it.
390 This may appear a formidable challenge but there is a precedence for it; an improvement
391 of the mirrors in the ring laser in 2009 led to a sudden improvement of the signal-to-noise
392 ratio approximately a factor of 10 [Hadziioannou et al., 2012] and removed the concerns
393 for small signals in ring laser data [Widmer-Schnidrig and Zürn, 2009].

394 **(5.3) Need for accurate local structure**

395 In our analysis, we relied on an earth model for WET in a model of the European
396 continent [Fichtner et al., 2013] because a regional model was not available. The quality
397 of our results hinges on the phase velocity for this model, as phase velocities are simply
398 multiplied to the rotation-rate data in order to obtain transverse acceleration.

399 This earth model was also used to compute the eigenfunctions of Rayleigh and
400 Love waves for the kinetic energy estimates. This model does not have a sedimentary
401 layer at top; however, if a low-velocity sedimentary layer existed at WET, it may affect
402 our energy estimates. This is because we determine surface amplitudes of Love and
403 Rayleigh waves from data and use them to infer the total energy of surface waves.

404 Fig. 12 shows the effects of sedimentary layer on the eigenfunctions when we
405 placed a sedimentary layer with a thickness of 250 m at the surface. This sedimentary
406 layer had P-wave velocity of 2 km/s and S-wave velocity of 1 km/s. Below 250 m, the
407 same structure with Fig. 6 (top) was kept for the computation. The solid lines are the
408 same eigenfunctions with those in Fig. 9 (anisotropic version) and the dashed lines are
409 the eigenfunctions for the modified structure with sediment. The eigenfunctions of
410 Rayleigh waves (U and V) change but their deviations are not systematic with depth.
411 Deviations are positive for some depths but are negative for other depths. On the other
412 hand, the eigenfunction of Love waves (W) becomes systematically smaller from the
413 presence of a sedimentary layer and this leads to a smaller estimate of Love-wave energy.
414 In this case, the Love-wave energy becomes 5-6 percent smaller. Considering the
415 uncertainties in our estimates for the energy ratios (~ 10 percent), this is a concern but is
416 not sufficiently large to change our conclusions.

417 If the thickness of this sedimentary layer can become thicker, we may need to
418 revise our estimate for the energy ratios. However, a report by Jena Geos Ingenieurbüro
419 (personal communication) stated that the thickness is less than 10 m. Also from an
420 independent H/V ratio measurements, a case for a thicker sedimentary layer is not likely
421 at WET; our measurement for H/V for the secondary microseism at WET indicates a ratio

of about 1/1.4, approximately 40 percent larger vertical amplitudes than horizontal amplitudes (in the Rayleigh-wave particle motion in the secondary microseism). Such a vertically elongated Rayleigh-wave particle motion indicates that the structure cannot have a thick sedimentary layer. In fact, this H/V ratio is fit quite well by the model of Fichtner et al. [2013] which does not have a sedimentary layer. Therefore, we believe our result of large Love-wave energy is still supported for WET. In general, we have not found any inconsistency between this earth model (Fig. 6) and other local data so far. But our results can be made more reliable if we can derive a local seismic structure using regional data sets. The key is in clarifying seismic velocity structure near the surface. We intend to do so in the future.

Acknowledgments

All data used in this study, ring laser data and STS-2 data at WET, are available from the GEOFON and EIDA data archives at www.webdc.eu. The operation of the ring laser is supported by the Bundesamt für Kartographie und Geodäsie (BKG). HI acknowledges support from the ERC Advanced Grant "ROMY", CH from grant HA7019/1-1 by the Emmy-Noether Programme of the German Research Foundation (DFG), and US and AG from grant Schr645/6-1 by the DFG. TT is grateful for a fellowship from the Center for Advanced Study at LMU, Munich, and is supported by NSF EAR-1547523. We thank M. Afanasiev and A. Fichtner for the seismic model at WET.

442 **References**

443 Ardhuin, F., L. Gualtieri, and E. Stutzmann (2015), How ocean waves rock the Earth:
444 Two mechanisms explain microseisms with periods 3 to 300 s, *Geophys. Res. Lett.,*
445 42(3), 765-772, doi:10.1002/2014GL062782.

446

447 Ben-Zion, Y. and A. A. Allam (2013), Seasonal thermoelastic strain and postseismic
448 effects in Parkfield borehole dilatometers, Earth Planet. Sci. Lett., 379, 120-126.

449

450 Chevrot, S., M. Sylvander, S. Benahmed, C. Ponsolles, J. M. Lefe'vre, and D. Paradis
451 (2007), Source locations of secondary microseisms in western Europe: Evidence for both
452 coastal and pelagic sources, J. Geophys. Res., 112, B11301, doi:10.1029/2007JB005059

453

454 Ferreira, A. and I. Igel (2009), Rotational motions of seismic surface waves in a laterally
455 heterogeneous Earth, Bull. Seism. Soc. Am., 99(2B), 1429-1436.

456

457 Fichtner, A., J. Trampert, P. Cupillard, E. Saygin, T. Taymaz, Y. Capdeville and A.
458 Villasenor (2013), Multiscale full waveform inversion, *Geophys. J. Int.,* 194, 534-556,
459 doi:10.1093/gji/ggt118

460

461 Friedrich, A., F. Kruger, and K. Klinge, Ocean-generated microseismic noise located
462 with the Grafenberg array, J. of Seismology, 2, 47-64, 1998.

463

464 Gualtieri, L., E. Stutzmann, Y. Capdeville, V. Farra, A. Mangeney, and A. Morelli
465 (2015), On the shaping factors of the secondary microseismic wavefield, *J. Geophys.*
466 *Res., Solid Earth,* 120, 6241-6262, doi:10.1002/2015JB012157
467
468 Hadziioannou, C., P. Gaebler, U. Schreiber, J. Wassermann, and H. Igel (2012),
469 Examining ambient noise using co-located measurements of rotational and translational
470 motion, *J. Seismol*., **16**, 787, doi:10.1007/s10950-012-9288-5.
471
472 Igel, H., U. Schreiber, A. Flaws, B. Schuberth, A. Velikoseltsev, and A. Cochard (2005),
473 Rotational motions induced by the M8.1 Tokachioki earthquake, September 25, 2003,
474 *Geophys. Res. Lett.,* 32, L08309, doi:10.1029/2004GL022336.
475
476 Igel H, Cochard A, Wassermann J, Flaws A, Schreiber U, Velikoseltsev A, Pham Dinh N
477 (2007) Broad-band observations of earthquake-induced rotational ground motions,
478 *Geophys. J Int.,* 168(1):182–196
479
480 Igel, H., M-F. Nader, D. Kurrle, A-M. G. Ferreira, J. Wassermann, and K. U. Schreiber
481 (2011), Observations of Earth's toroidal free oscillations with a rotation sensor: The 2011
482 magnitude 9.0 Tohoku-Oki earthquake, *Geophys. Res. Lett*. **38**, L21303,
483 doi:10.1029/2011GL049045
484
485 Juretzek, C., M. Perleth, and C. Hadziioannou (2015), Characteristics of Love and
486 Rayleigh waves in ambient noise: wavetype ratio, source location and seasonal behavior,

Paper S41B-2759, AGU Fall Meeting.

Kobayashi, N. and K. Nishida (1998), Continuous excitation of planetary free oscillations by atmospheric disturbances, *Nature,* 395, 357-360.

Kurrle, D. and R. Widmer-Schnidrig (2008). The horizontal hum of the Earth: a global background of spheroidal and toroidal modes, *Geophys. Res. Lett.,* **35**(6), L06304, doi:10.1029/2007GL033125.

Kurrle, D., H. Igel, A-M. G. Ferreira, J. Wassermann, and U. Schreiber (2010), Can we estimate local Love wave dispersion properties from collocated amplitude measurements of translations and rotations?, *Geophys. Res. Lett*., **37**(4), 1, doi:10.1029/2009GL042215

Longuet-Higgins, M. (1950), A theory of the origin of microseisms. *Phil. Trans. R. Soc. Lond., Ser A*, *Math. Phy.s Sci.,* 243(857), 1–35.

Nishida K, Kawakatsu H, Fukao Y, Obara K (2008) Background Love and Rayleigh waves simultaneously generated at the Pacific Ocean floors, *Geophys. Res. Lett.,* 35(16):1–5

Osaki, Y. (1976), *Introduction to spectral analysis for seismic ground motion* (in Japanese), Kajima Publishing Co., Tokyo.

510 Pancha A., T.H. Webb, G. E. Stedman,D. P. McLeod, and K. U. Schreiber (2000), Ring
511 laser detection of rotations from teleseismic waves, *Geophys Res Lett* 27(21):3553
512
513 Pham N., H. Igel, J. Wassermann, Kaser M, de La Puente J, Schreiber U (2009)
514 Observations and modeling of rotational signals in the P-coda: constraints on crustal
515 scattering, *Bull. Seism. Soc. Am.,* 99(2B):1315
516
517 Prawirodirdjo, L., Y. Ben-Zion and Y. Bock (2006), Observation and modeling of
518 thermoelastic strain in Southern California Integrated GPS Network daily position time
519 series, J. Geophys. Res., Solid Earth, 111, B02408, doi:10.1029/2005JB003716.
520
521 Riahi, N., G. Bokelmann, P. Sala and E. H. Saenger (2013), Time-lapse analysis of
522 ambient surface wave anisotropy: A three-component array study above an underground
523 gas storage, J. Geophys. Res., Solid Earth, 118, 5399-5351, doi:10.1012/jgrb.50375
524
525 Saito, T. (2010), Love-wave excitation due to the interaction between a propagating
526 ocean wave and the sea-bottom topography, Geophys. J. Int., 182, 1515-1523,
527 doi:10.1111/j.1365-246X.2010.04695.x
528
529 Schreiber, U., and J.-P. Wells (2013), Invited Review Article: Large ring laser for
530 rotation sensing, *Rev. Sci. Instrum*., 84, 041101, doi:10.1063/1.4798216
531
532 Schreiber, U., J. N. Hautmann, A. Velikoseltsev, J. Wassermann, H. Igel, J. Otero, F.

533 Vernon, and J.‐P. R. Wells (2009), Ring laser measurements of ground rotations for
534 seismology, *Bull. Seism. Soc. Am.,* 99(2B), 1190–1198, doi:10.1785/0120080171
535
536 Suda, N., K. Nawa, and Y. Fukao (1998), Earth's background free oscillations, *Science,*
537 279, 2089-2091.
538
539 Takeuchi, H. and M. Saito (1972), Seismic Surface Waves, in Methods in Computational
540 Physics, vol. 11, 217-295.
541
542 Tanimoto, T., C. Hadziioannou, H. Igel, J. Wasserman, U. Schreiber, and André Gebauer,
543 Estimate of Rayleigh-to-Love wave ratio in the secondary microseism by colocated ring
544 laser and seismograph, *Geophys. Res. Lett*., 42, doi:10.1002/2015GL063637
545
546 Tanimoto, T., J. Um, K. Nishida and N. Kobayashi (1998), Earth's continuous
547 oscillations observed seismically quiet days, *Geophys. Res. Lett.,* 25, 1553-1556.
548
549 Widmer-Schnidrig, R., and W. Zürn (2009), Perspectives for ring laser gyroscopes in
550 low-frequency seismology. *Bull. Seism. Soc. Am.,* 99(2B):1199
551

552 **Figure Captions**

553 **Fig. 1**. Station WET (Wettzell) is indicated by the red mark, close to the German-Czech
554 border.

555 **Fig. 2a:** Power Spectral Density (PSD) of rotation rate (0.1-0.4 Hz), recorded by the ring
556 laser at Wettzell. Each point was computed from a 15-minute long time series. Unit is
557 nano-radians^2 /sec. Data from 2009 to 2015 are folded onto one year using the Julian
558 days.

559 **Fig. 2b**: **(Left)** Monthly averages of the ring laser data; the mean and one-sigma standard
560 deviation of the power spectral density (for frequencies 0.10-0.40 Hz) are shown. The
561 abscissa is month in number. **(Right)** Monthly averages of the vertical component
562 seismic data under the same conditions with ring laser data.

563 **Fig. 3**: Monthly averages of Fourier spectral amplitude (normalized by the length of time
564 series) for vertical-component seismograms after removal of earthquake effects. The
565 numbers are used to denote months. For example, 1 is January, 2 is February and so forth.
566 Winter months (1, 2, 12) are in blue, summer months (6, 7, 8) are in red, spring months
567 (3, 4, 5) are in green, and fall months (9, 10, 11) are in yellow with black circles.

568 **Fig. 4**: Same as Fig. 3 except that this is for monthly averages of ring laser data. We find
569 the minimum resolution limit in data (horizontal dash) which makes it difficult to study
570 the primary microseism (0.05-0.07 Hz). This study focused on the secondary microseism
571 for frequencies 0.13-0.30 Hz.

572 **Fig. 5:** Using the average PSDs in 2010 (Julian days from 214 to 226), shown by red box
573 in the top panel, Fourier spectral amplitudes are plotted in the bottom panel. Near

574 constant amplitudes in the low frequency range (up to about 0.15 Hz in the bottom panel)
575 is due to this minimum resolution limit. We determined this level and subtracted it from
576 the ring laser data.

577 **Fig. 6: (top)** P-wave and S-wave structure at WET from a model of European continent
578 (Fichtner et al., 2013). The right edge is the Earth's surface (radius 6371 km) and PV, PH
579 and SV and SH velocities are shown. The abscissa is the radius from the center of the
580 Earth. **(bottom)** Love-wave fundamental-mode phase velocity computed for this model.
581 The abscissa is frequency (Hz) and the ordinate is phase velocity (km/s).

582 **Fig. 7:** Transverse accelerations from ring laser are shown in red (pure SH signals).
583 Vertical, NS, EW accelerations are shown in blue, green and black, respectively. Results
584 for January (month 1, top-left), April (month 4, top-right), July (month 7, bottom-left),
585 and October (month 10, bottom-right) are shown.

586 **Fig. 8: (top)** Surface acceleration ratios between vertical acceleration and transverse
587 acceleration. Each curve is for a month and is denoted by the same color scheme. These
588 values are the ratios between the blue curves to the red curves in Fig. 7. **(bottom)** The
589 kinetic-energy ratios between Rayleigh waves and Love waves. Same color scheme with
590 Fig. 3 is used for each month.

591 **Fig. 9:** Examples of the eigenfunctions at 0.20 Hz used for computations of kinetic
592 energy ratios. The seismic model in Fig. 6 was used. Red is the eigenfunction (W) for
593 Love waves (fundamental mode) and blue and green curves are the eigenfunctions (U and
594 V) for Rayleigh waves (fundamental mode). Solid lines are for the original anisotropic
595 model by Fichtner et al. (2013) while dashed lines are for the averaged isotropic model.
596 Effects of anisotropy are not important for our results.

Fig. 10: Monthly variations in the kinetic-energy ratios between Rayleigh waves and Love waves (E_R/E_L). Blue is for the frequency range 0.13-0.25 Hz where the amplitude peaks are found. Red is for the frequency range 0.13-0.30 Hz. Both data show relatively stable values throughout a year except for June and July. Error bars are only shown for 0.13-0.25 Hz in order to reduce clutter but they are similar for 0.13-0.30 Hz.

Fig. 11: Effects of the baseline values (threshold) on the kinetic-energy ratios. Two cases (0.7 and 0.8) are shown. Our preferred value for the baseline is 0.75-0.80 (prad/s). Higher ratios in June and July are affected by this choice but within our preferred values, the ratio shows a sudden increase. Error bars are only given for the blue curve but they are quite similar for the red curve.

Fig. 12: Effects of a shallow low-velocity layer on the eigenfunctions. Solid lines are the same with Figure 9 (anisotropic case). Dashed lines are the eigenfunctions for a structure with a low-velocity sedimentary layer in the upper 250 m. P-wave velocity is 2 km/s, S-wave velocity is 1 km/s and density is 2300 kg/m^3 in this layer.

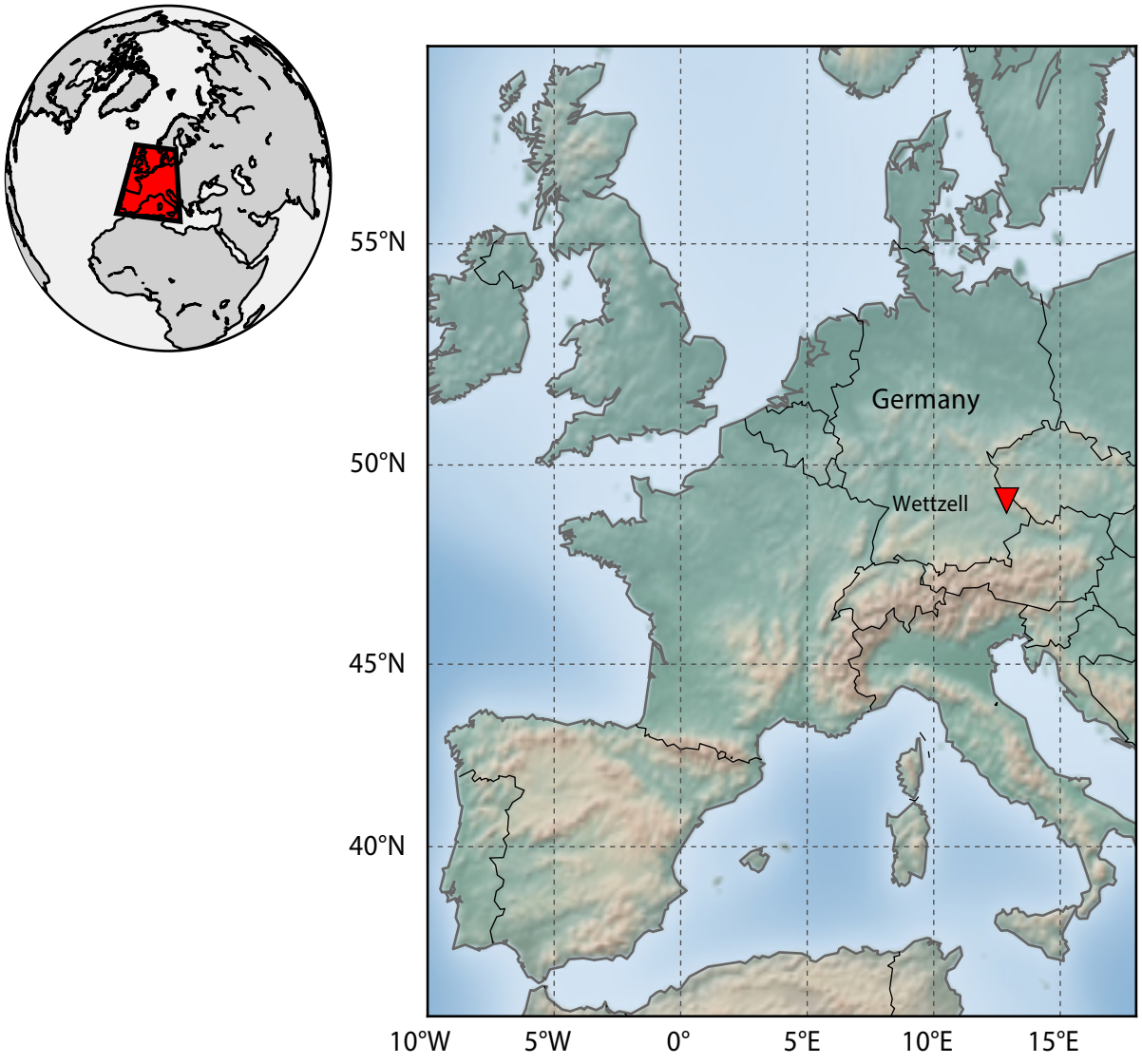

Figure 1

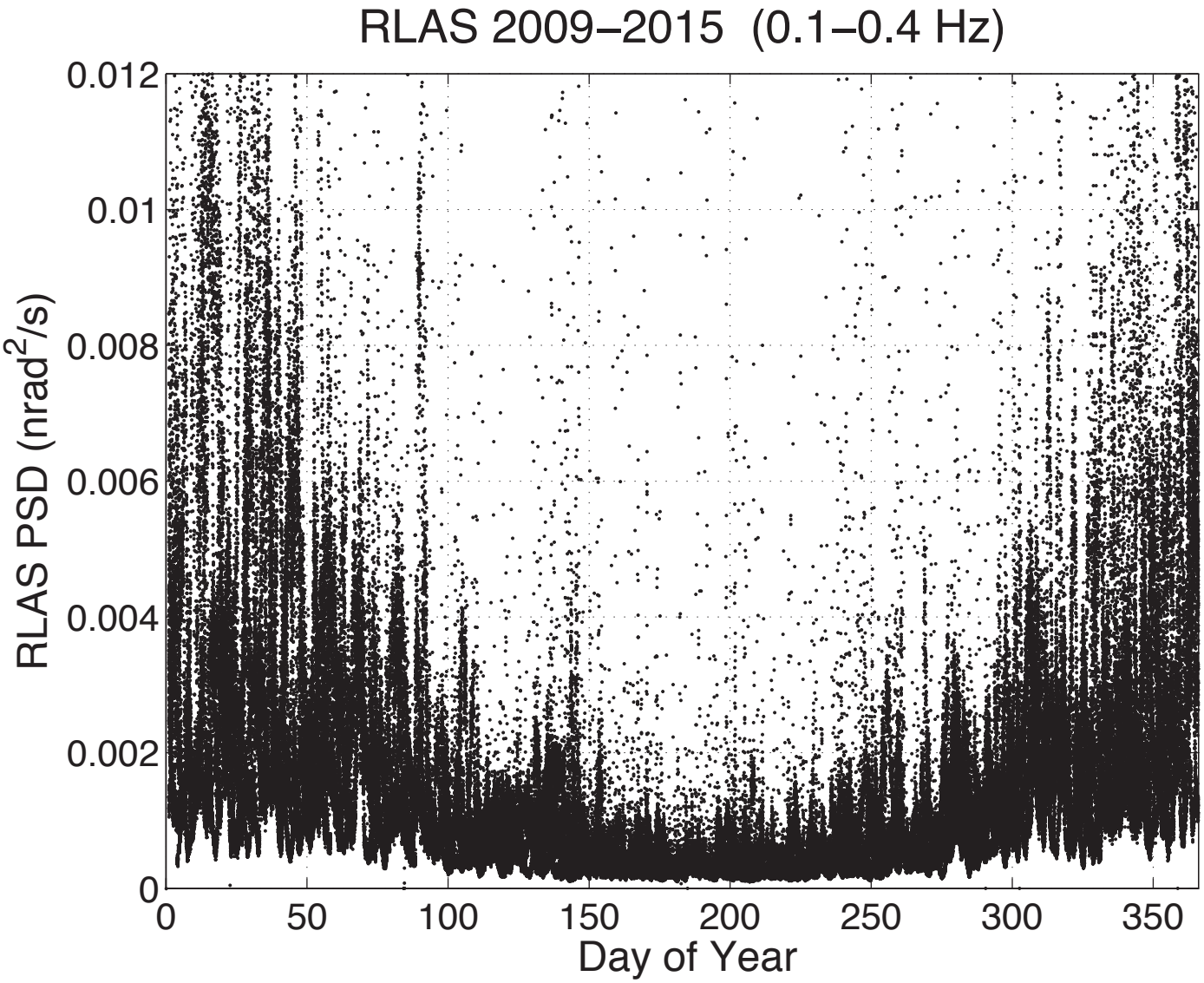
RLAS 2009–2015 (0.1–0.4 Hz)
RLAS PSD (nrad²/s)
0.012
0.01
0.008
0.006
0.004
0.002
0
0
50
100
150
200
250
300
350
Day of Year

Figure 2a

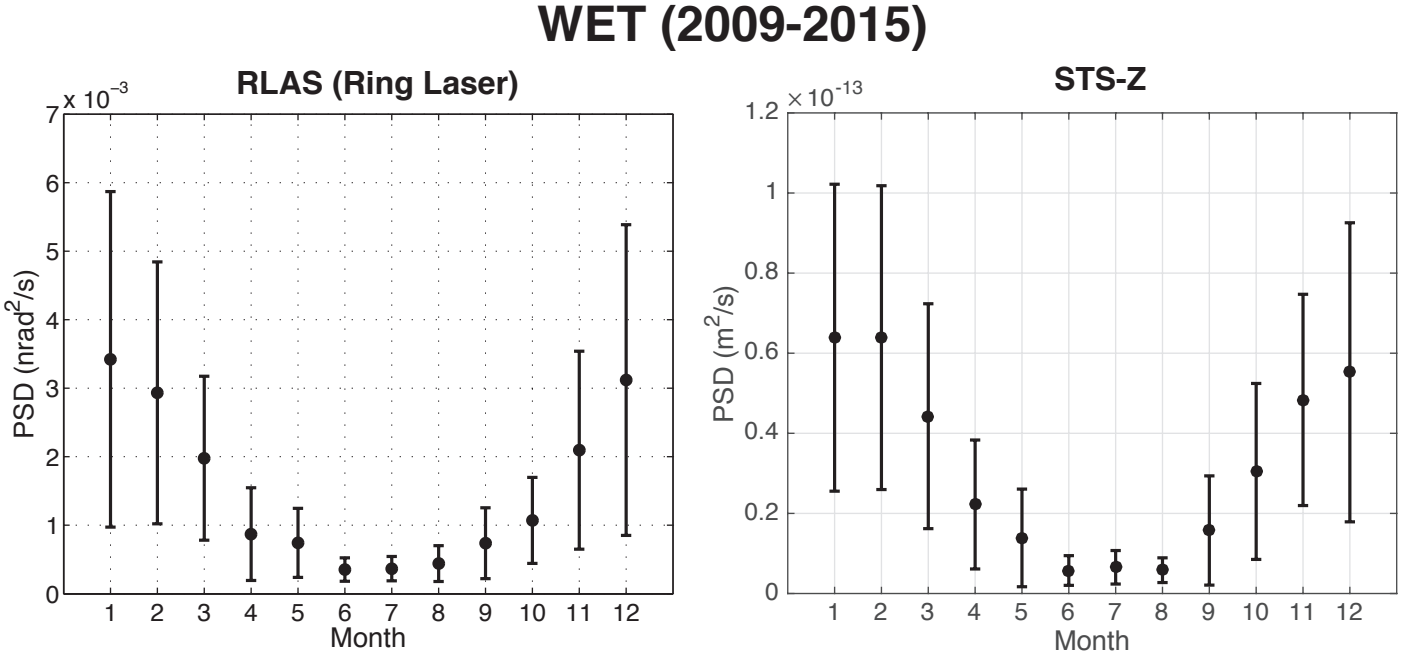
WET (2009-2015)
RLAS (Ring Laser)
x 10^-3
PSD (nrad^2/s)
Month
STS-Z
×10^-13
PSD (m^2/s)
Month

Figure 2b

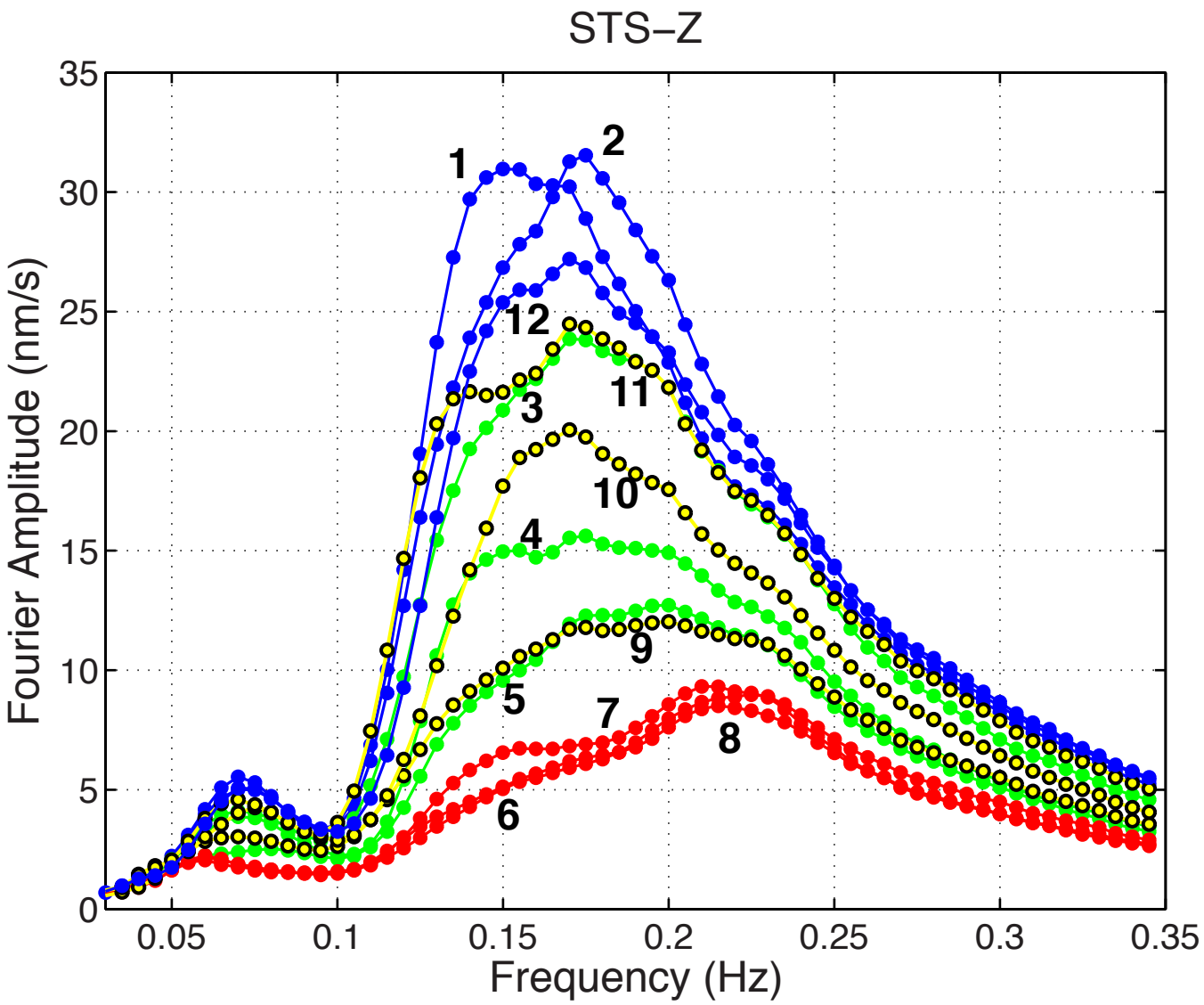
STS–Z
Fourier Amplitude (nm/s)
Frequency (Hz)
0
5
10
15
20
25
30
35
0.05
0.1
0.15
0.2
0.25
0.3
0.35
1
2
12
11
3
10
4
9
5
7
8
6

Figure 3

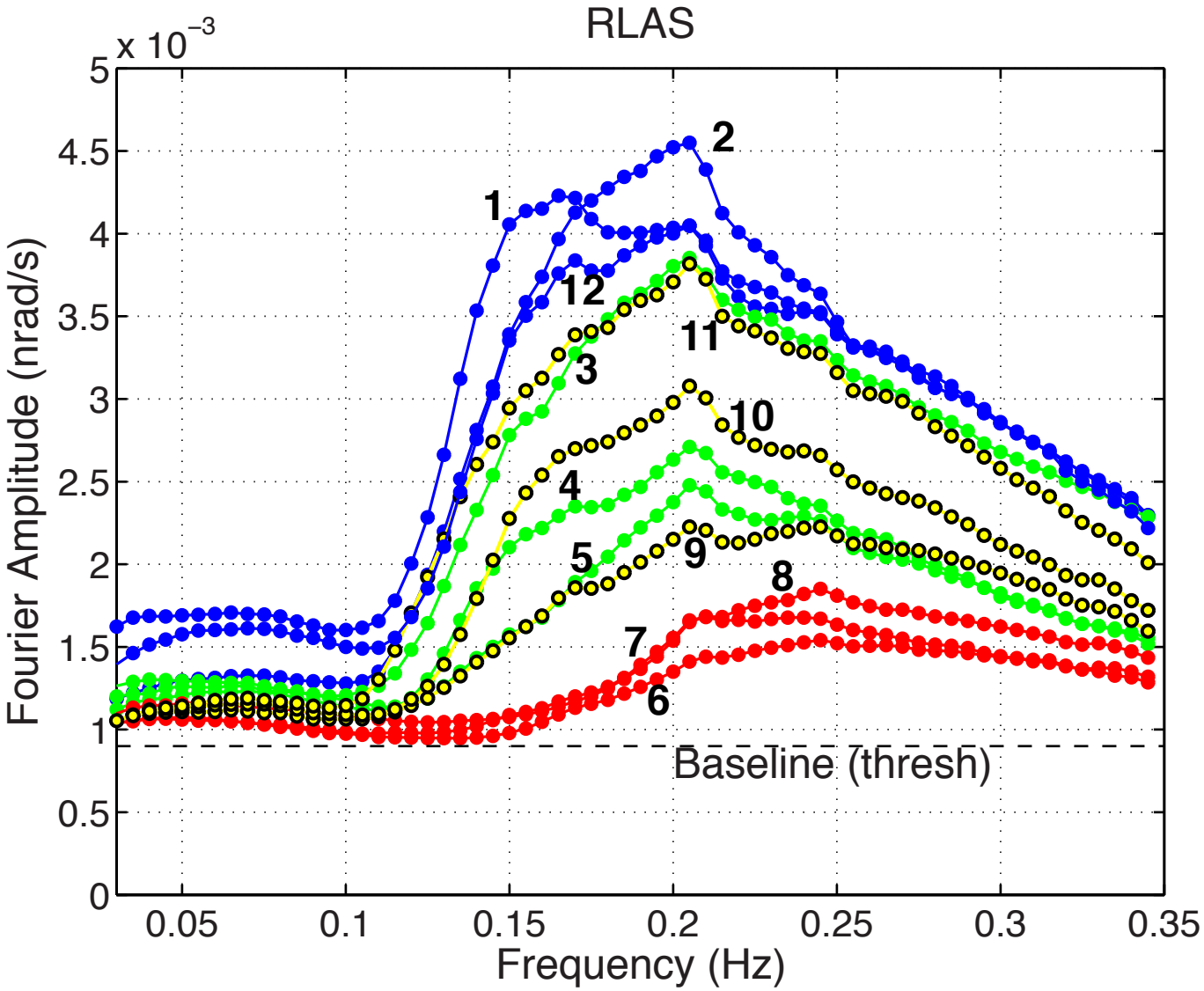
RLAS
x 10^−3
Fourier Amplitude (nrad/s)
Frequency (Hz)
Baseline (thresh)
1
2
3
4
5
6
7
8
9
10
11
12
0
0.5
1
1.5
2
2.5
3
3.5
4
4.5
5
0.05
0.1
0.15
0.2
0.25
0.3
0.35

Figure 4

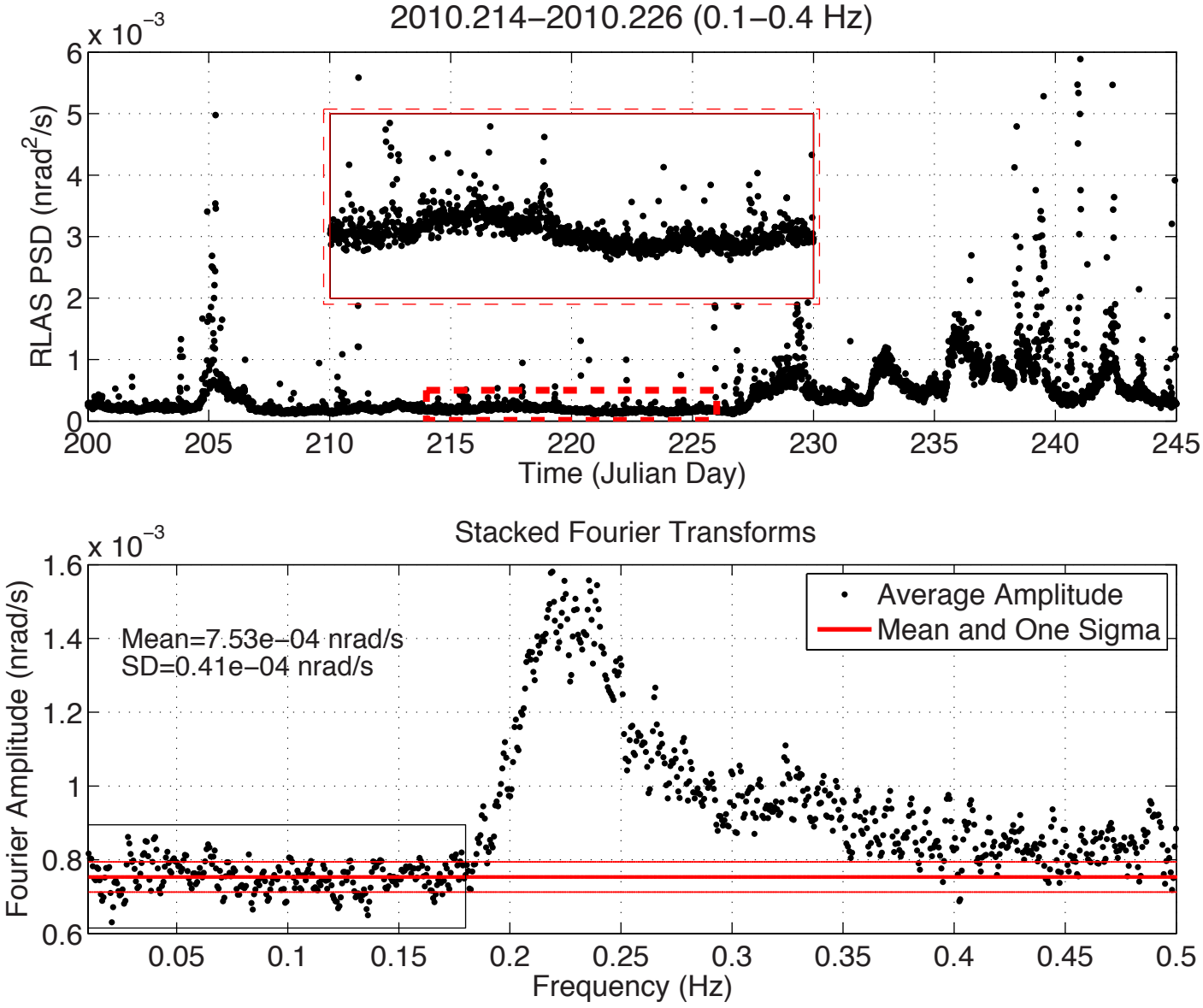
2010.214–2010.226 (0.1–0.4 Hz)
x 10^−3
RLAS PSD (nrad^2/s)
Time (Julian Day)
Stacked Fourier Transforms
Fourier Amplitude (nrad/s)
Mean=7.53e−04 nrad/s
SD=0.41e−04 nrad/s
Average Amplitude
Mean and One Sigma
Frequency (Hz)

Figure 5

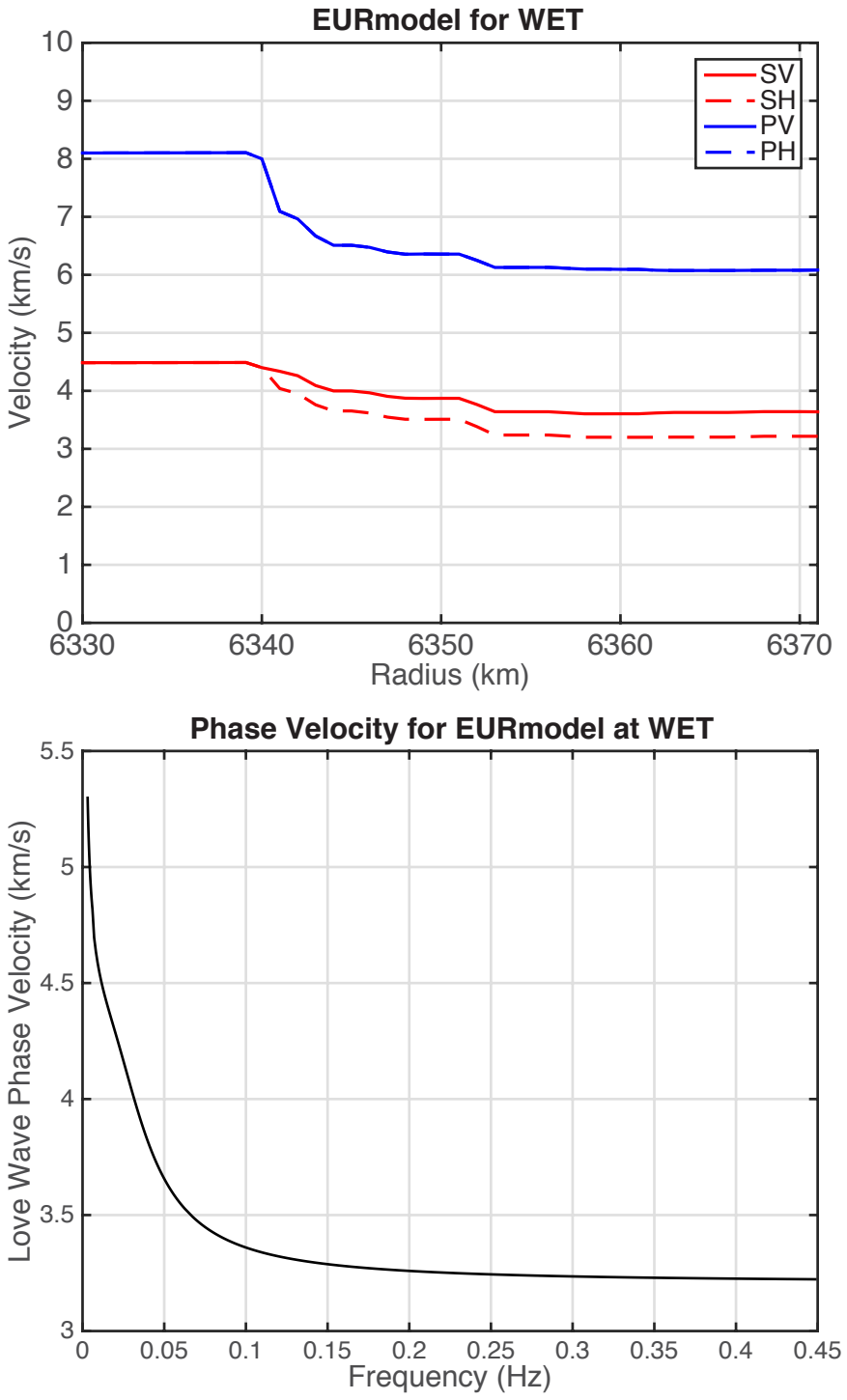
EURmodel for WET
SV
SH
PV
PH
Velocity (km/s)
Radius (km)
10
9
8
7
6
5
4
3
2
1
0
6330
6340
6350
6360
6370
Phase Velocity for EURmodel at WET
Love Wave Phase Velocity (km/s)
Frequency (Hz)
5.5
5
4.5
4
3.5
3
0
0.05
0.1
0.15
0.2
0.25
0.3
0.35
0.4
0.45

Figure 6

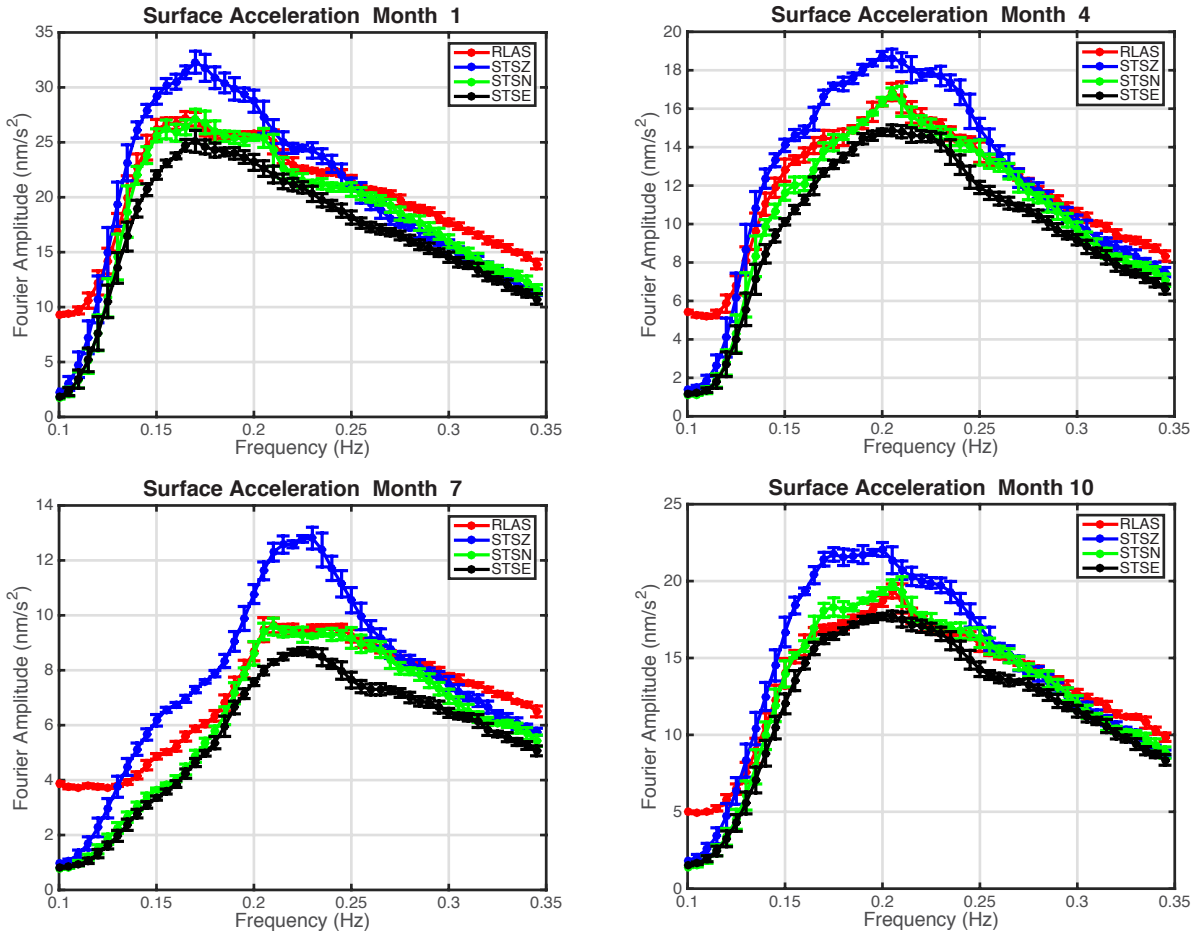
Surface Acceleration Month 1
Surface Acceleration Month 4
Surface Acceleration Month 7
Surface Acceleration Month 10
RLAS
STSZ
STSN
STSE
Fourier Amplitude (nm/s^2)
Frequency (Hz)

Figure 7

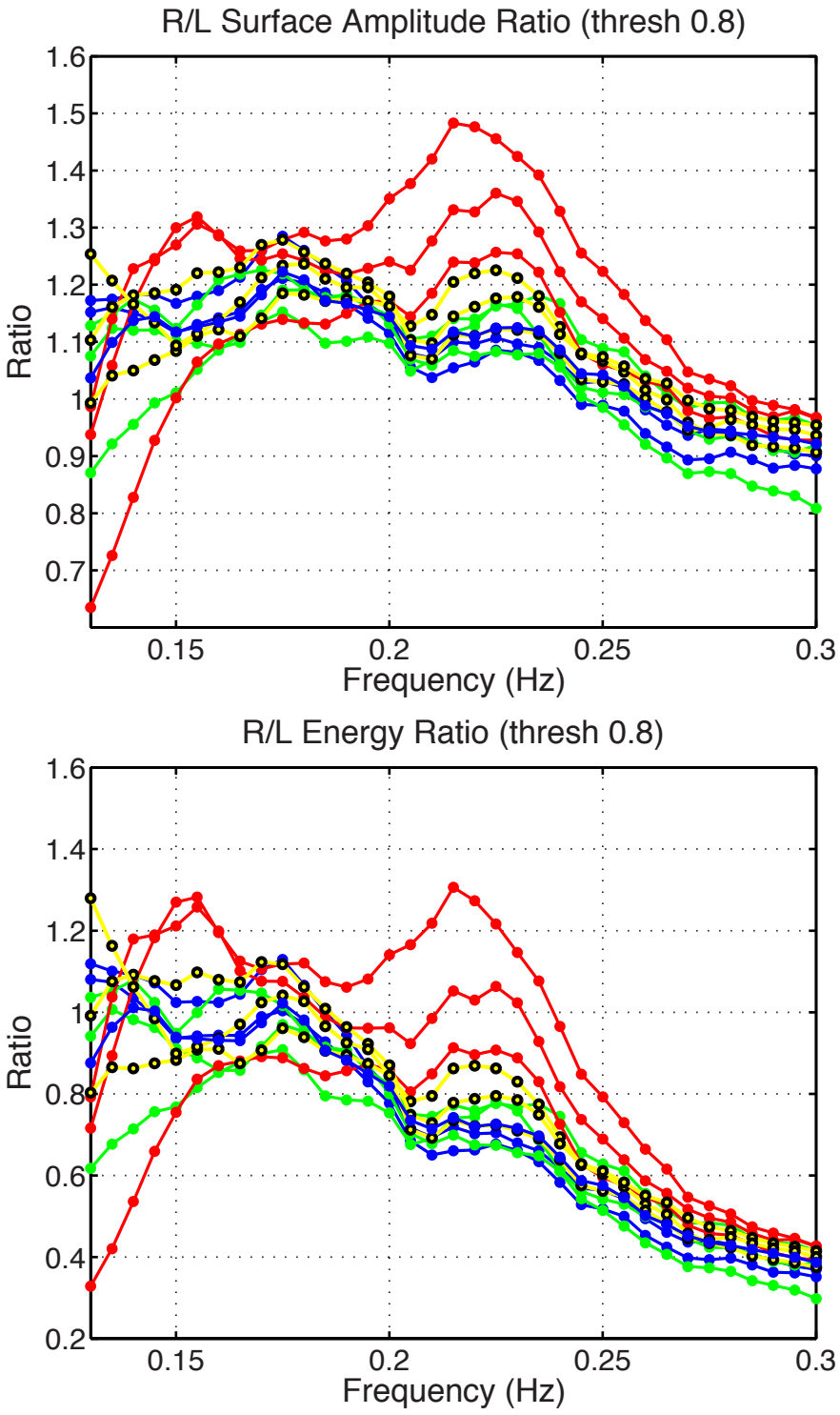
R/L Surface Amplitude Ratio (thresh 0.8)
Ratio
Frequency (Hz)
R/L Energy Ratio (thresh 0.8)
Ratio
Frequency (Hz)

Figure 8

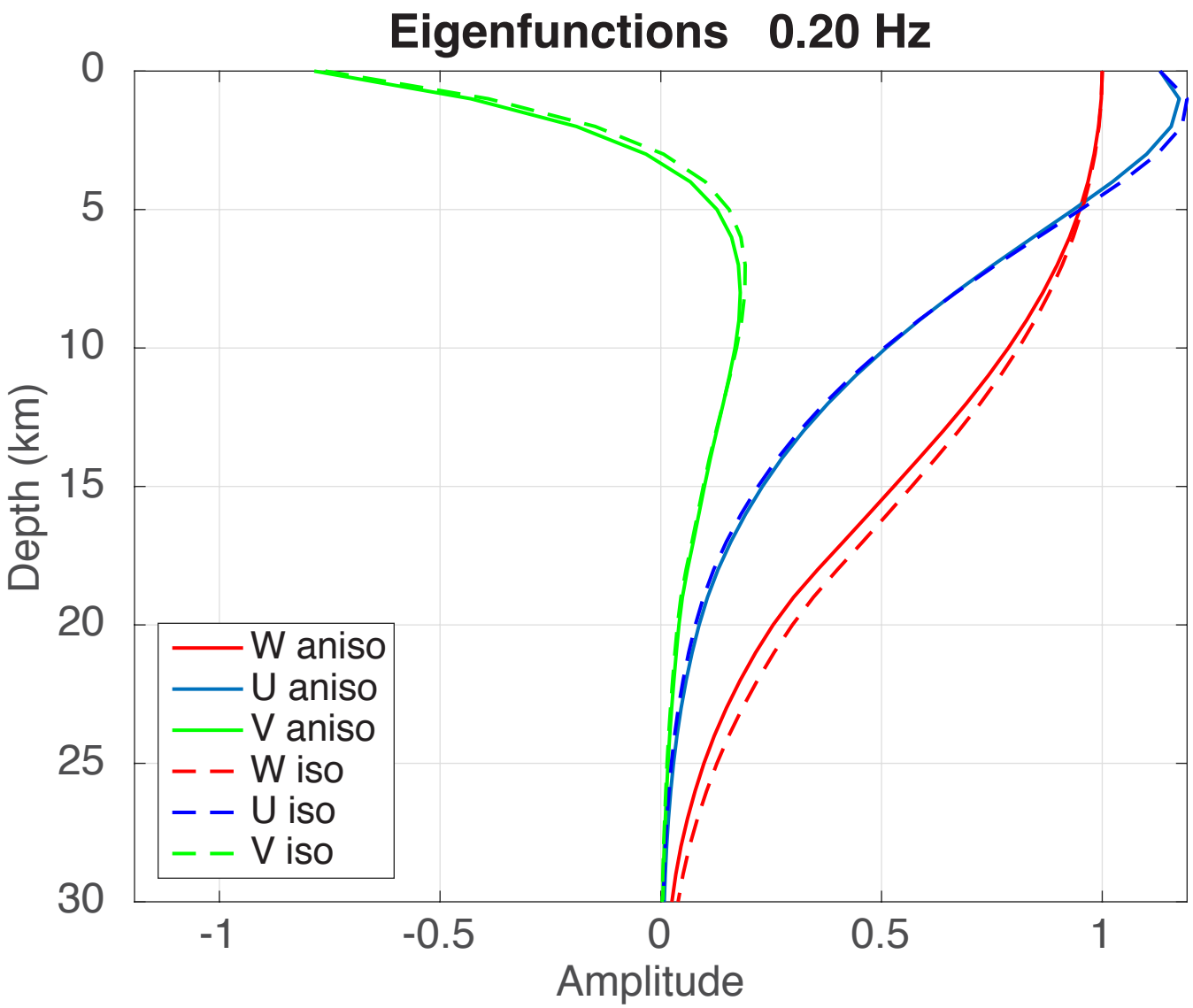
Eigenfunctions 0.20 Hz
Depth (km)
0
5
10
15
20
25
30
-1
-0.5
0
0.5
1
Amplitude
W aniso
U aniso
V aniso
W iso
U iso
V iso

Figure 9

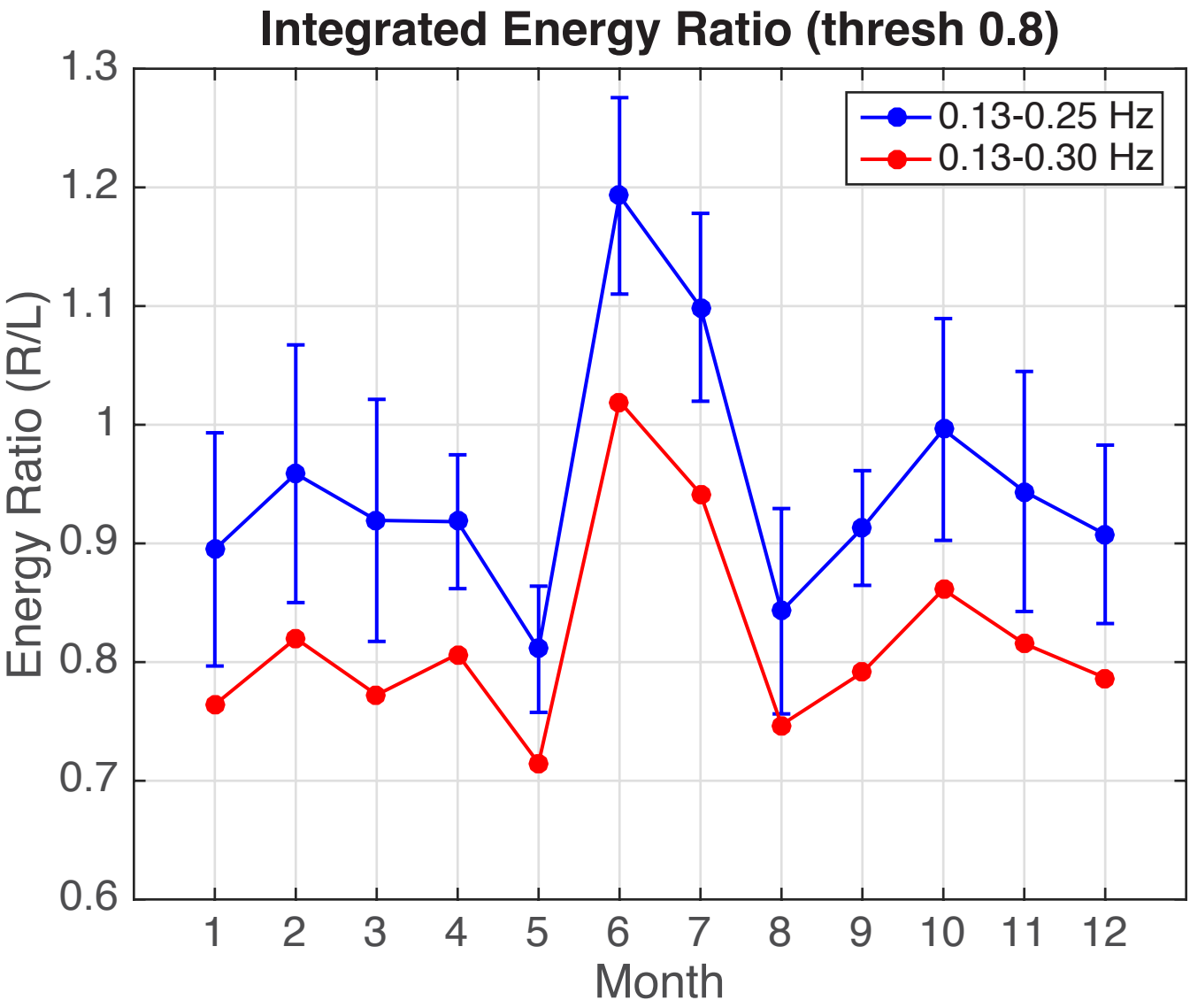
Integrated Energy Ratio (thresh 0.8)
0.13-0.25 Hz
0.13-0.30 Hz
Energy Ratio (R/L)
1.3
1.2
1.1
1
0.9
0.8
0.7
0.6
1
2
3
4
5
6
7
8
9
10
11
12
Month

Figure 10

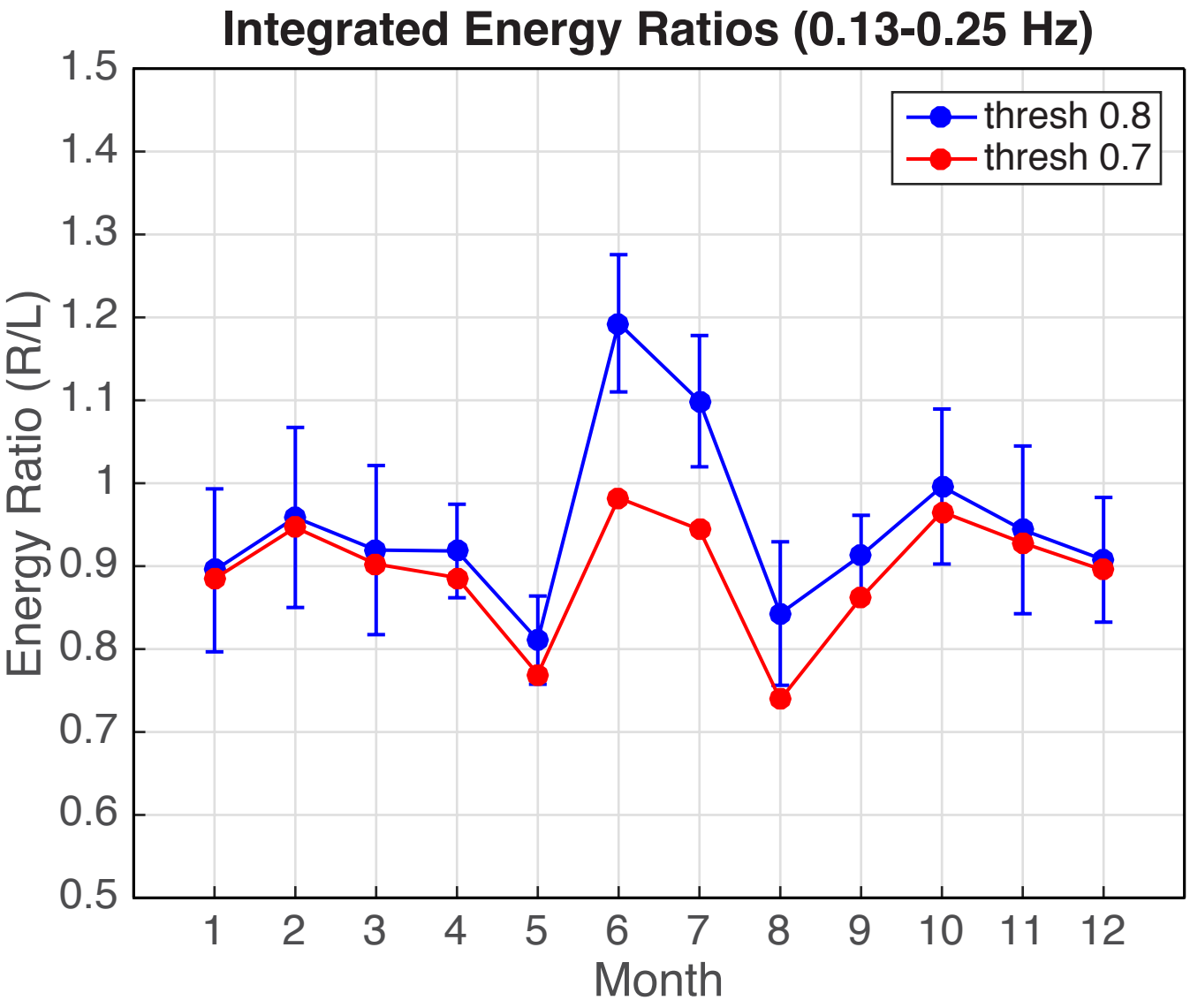
Integrated Energy Ratios (0.13-0.25 Hz)
thresh 0.8
thresh 0.7
Energy Ratio (R/L)
1.5
1.4
1.3
1.2
1.1
1
0.9
0.8
0.7
0.6
0.5
1
2
3
4
5
6
7
8
9
10
11
12
Month

Figure 11

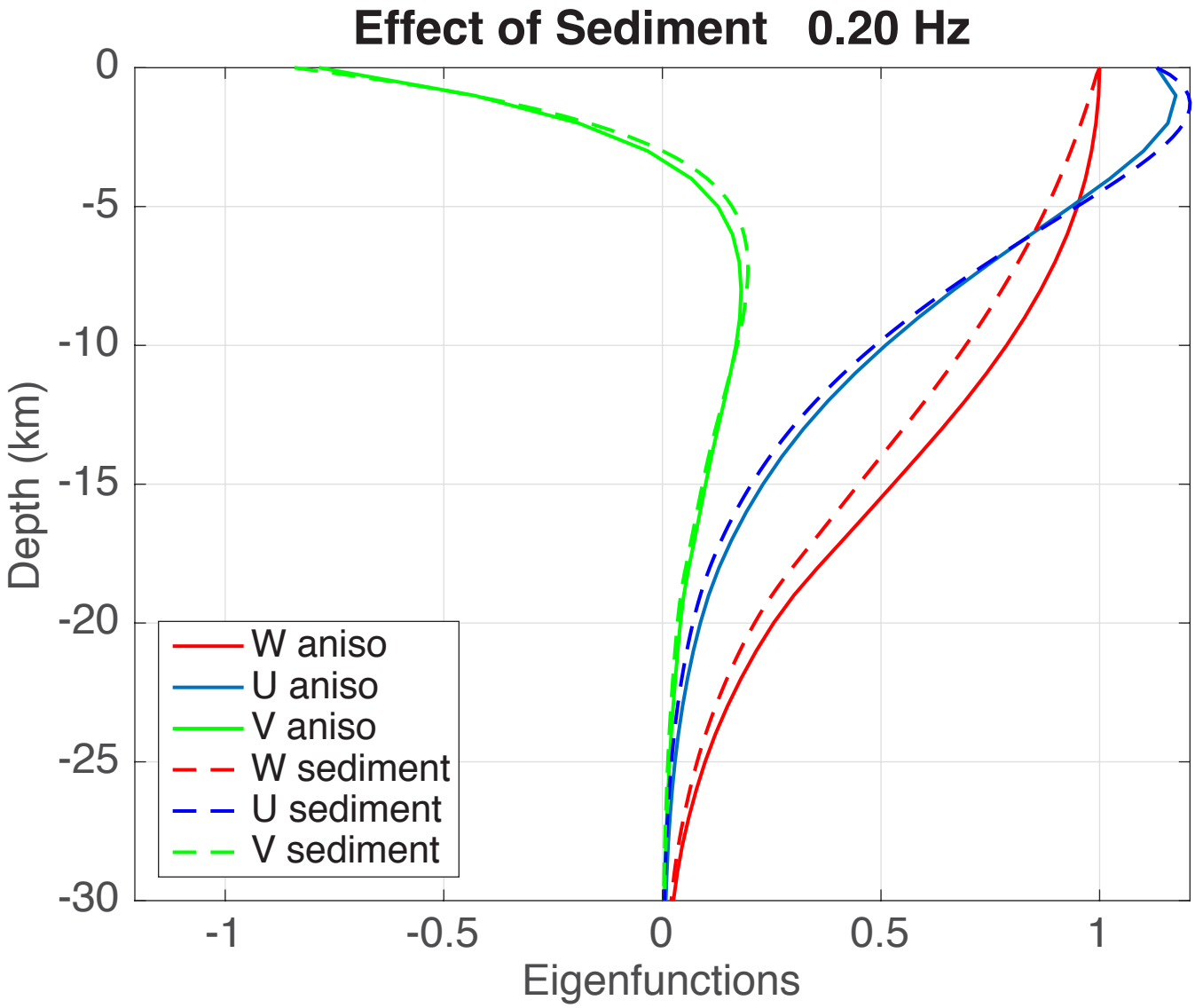
Effect of Sediment 0.20 Hz
0
-5
-10
-15
-20
-25
-30
Depth (km)
-1
-0.5
0
0.5
1
Eigenfunctions
W aniso
U aniso
V aniso
W sediment
U sediment
V sediment

Figure 12